Regenerative Neural Network (ReGeNN) for Rotating Scatter Mask Radiation Imaging

Robert J. Olesen[a], James B. Cole[b], Darren E. Holland[a], Erik M. Brubaker[c], James E. Bevins[a]

[a]*Robert.Olesen@afit.edu*
Department of Engineering Physics
Air Force Institute of Technology
Wright-Patterson AFB, OH 45433 USA
[b]*Department of Physics*
Bard College
Washington, DC 20019 USA
[c]*Sandia National Laboratories*
Livermore, CA 94720 USA

Abstract

In this paper, a regenerative neural network (ReGeNN) was designed and tested for application to rotating scatter mask (RSM) gamma imaging. The network was trained using detector responses for a variety of realistic source distributions simulated in MCNP v6.1.4. ReGeNN was shown to reconstruct the source images with excellent quality when trained under ideal conditions. When comparing to standard Maximum Likelihood-Expectation Maximization algorithms, ReGeNN reduced the relative error from 145% to just 33% and increased the precision from 27 to 85% averaged over the 27 test source distributions. The network also demonstrated robust learning capabilities after successfully training on noisy input data, with only relatively minor degradation to the source reconstruction quality. An analysis of variance study determined that the most significant factor affecting the reconstruction quality was the source's shape, with ring-type source distributions having the worst performance. The interaction between the source's size and direction was also discovered to have a small effect as larger sources located near the bottom of the system's field-of-view contained more phantoms within the reconstruction. The results show a significant improvement over more conventional algorithms, suggesting that real-time imaging with the RSM may not only be plausible, but practical for the first time. ReGeNN may readily be adapted for similar time-encoded radiation imaging systems, but the neural network methods described also have significant application potential towards nuclear security and safety.

Keywords:
Radiation Imaging, Machine Learning, Neural Network, Gamma Rays, Rotating Scatter Mask

1. Introduction

Monitoring, localizing, and characterizing radioactive sources remains a priority in applications for nuclear security and safety [1, 2, 3, 4]. Radiation imaging has become a staple in the biomedical community, but such advances resulted from the source's well-defined and constrained nature in such applications. For nuclear security and safety,

the composition and location of the source is not necessarily constrained, and interference from environmental shielding and noise further complicates the ability to monitor, localize, and/or characterize radioactive sources. Overcoming these challenges requires devices with large field-of-views (FOV), high detection efficiencies, and large signal-to-noise ratios (SNR), but these parameters are often in direct conflict with each other. Traditional coded-aperture systems are often limited in FOV and efficiency [5], although recent developments have shown some improvements through alternative detector arrangements and reconstruction algorithms [6, 7]. Compton cameras continue to have excellent SNR and FOV, but at a higher cost to efficiency and being unable to perform dual-particle imaging [5, 8, 9, 10]. Building on the principles from Compton cameras, novel dual-particle scatter cameras are currently being investigated that may remedy some of these limitations [11, 12].

This study evaluates an alternative, novel imaging approach through the rotating scatter mask (RSM) system. Previous development and evaluation has demonstrated the RSM as a directional, dual-particle detection system with relatively high detection efficiencies and nearly full 4π FOV [13, 14, 15, 16, 17]. A previous study indicated that gamma imaging may be possible through appropriate reconstruction algorithms, without requiring any changes to the physical setup or data collection [18]. However, that study discovered that the maximum-likelihood expectation-maximization (ML-EM) algorithm, a technique often used throughout a variety of the radiation imaging systems, failed to accurately reconstruct most source images, indicating that alternative priors or more advanced algorithms are required in regards to RSM imaging capabilities.

Artificial neural networks are prime candidates for this task, particularly convolutional neural networks (CNN) designed specifically for image reconstruction and deconvolution [19]. While a CNN architecture has been proposed and successfully integrated for a coded-aperture system [7], there relatively little literature regarding appropriate design and training for CNN in application to radiation imaging as compared to the comprehensive list of studies for more conventional algorithms such as ML-EM. In this paper, a novel CNN encoder-decoder architecture is proposed as an alternative imaging algorithm for the RSM system, which can be easily modified to fit other radiation imaging applications. Emphasis was given in describing the CNN architecture, with all hyper-parameters defined and outlined for readers to successfully reproduce and alter the design for specific radiation imaging applications. The imaging performance with the proposed CNN architecture is compared to the previous study using ML-EM as a benchmark to highlight increased image reconstruction performance.

2. Rotating Scatter Mask Imaging

The RSM system uses a spatially-varying attenuator, referred to as the mask, surrounding a standard scintillating detector, as shown in Figure 1a. The mask is connected to a motor so that it rotates along the detector's longitudinal
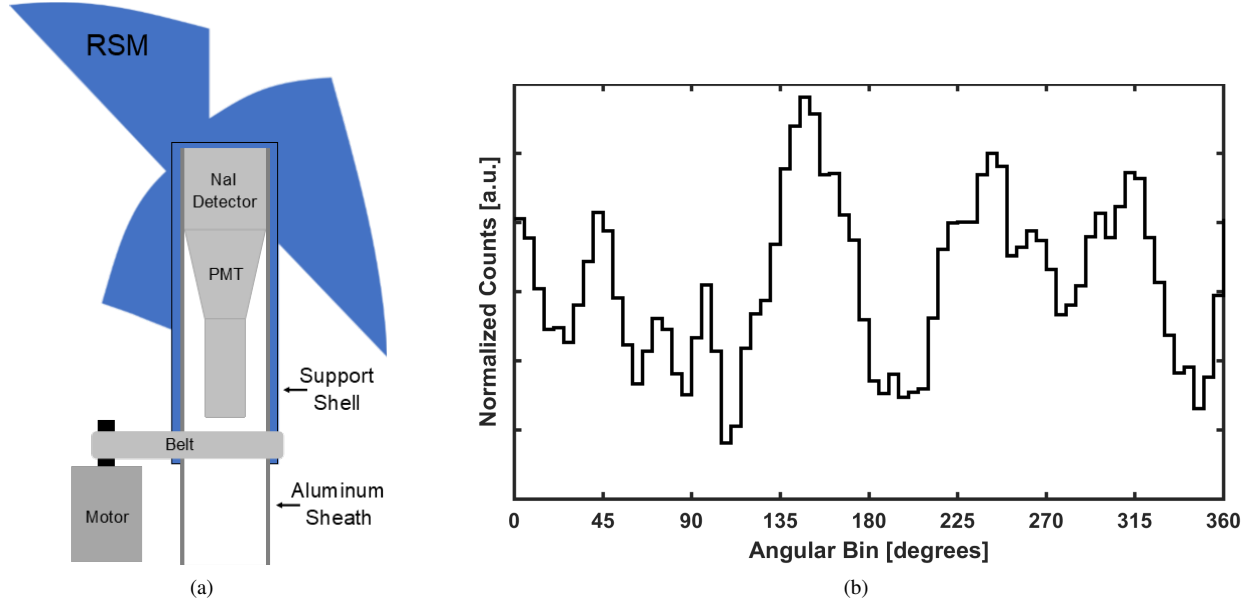
Figure 1: Schematic showing the RSM system's primary components (left) [15]. An acrylic-like mask (labelled RSM) slides over an aluminum sheath surrounding a scintillating detector and is attached to a motor so that it may freely rotate about the detector, generating a time-varying DRC (right).

axis; in the presence of a stationary radioactive source, this rotation generates a periodic, time-varying detector response. A detector response curve (DRC) is generated by recording the detected events versus rotation angle (Figure 1b), which ideally can be used to reproduce the source image. This process is similar to other time-encoded directional imaging systems [20, 21, 22], although these systems use a coded-aperture approach whereas the RSM system contains a much more complex mask design to theoretically improve imaging capability and FOV.

For this study, the mask design known as the "Mace" was chosen, in accordance with the ML-EM study previously mentioned [18]. The Mace geometry is shown in Figure 2. The DRCs were generated using the full-energy peak from a ^{137}Cs-simulated 662 keV point source located 86.36 cm from the center of a 3" x 3" NaI(Tl) detector, modeled in MCNP v6.1.4. The DRCs span from 5° - 170° in the polar angle ϕ (referenced from the axis of rotation) and 0° - 360° in the azimuthal (rotational) angle θ, both in 5° increments for a total of 2,448 point source directions and corresponding DRCs. Distributed sources were modeled as a collection of point sources; the total detector response was modeled as a weighted sum of the individual point source DRCs [18].

3. Methodology

Artificial neural networks have successfully been integrated into gamma and neutron spectroscopy [23, 24], and a recent study has demonstrated their potential in radiation imaging for coded-aperture systems [7]. Of interest to this study is the CNN due to its rising popularity as the state-of-the-art for image deconvolution and generation [25, 19].
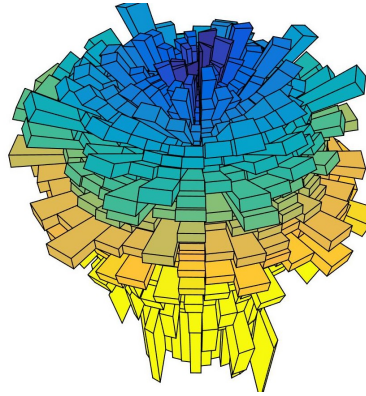
Figure 2: Design for the Mace RSM. The complex geometry theoretically improves the imaging capability compared to previously-explored "Spartan" RSM designs.

The proceeding section describes a novel CNN architecture that adapts the approach designed for computer vision image generation into a radiation image reconstruction algorithm.

3.1. Neural Network Architecture

The CNN architecture used for RSM imaging is shown in Figure 3, which borrows heavily from generative CNNs [25]. The generative CNN is designed to create generic classes of images (such as chairs, tables, and cars) using a random one-dimensional input array. However, a CNN for radiation imaging must generate a specific image given a measured DRC, similar to the principle behind the ML-EM algorithm which converges to the solution that has the maximum probability given the measured DRC. In other words, the generative CNN's purpose is to just generate a "realistic" image with no regards to the input, while RSM imaging requires one-to-one correspondence between the input and output through training on realistic source distributions. This difference is subtle, but plays a crucial role when considering appropriate training data and network design. To distinguish this neural network in application to radiation imaging, this proposed architecture will be referred to as the regenerative neural network (ReGeNN) throughout this study.

ReGeNN is composed of 9 total layers, split into an "encoder-decoder" format with the one-dimensional DRC as the input and the two-dimensional source reconstruction as the output. The first 5 layers form the "encoder" portion, using fully-connected layers (labelled FC), while the other 4 layers use a combination of upsampling and convolution to form the convolutional transpose layers (labelled CTr) that comprise the "decoder" portion.

To convert between the one-dimensional encoder to the two-dimensional image, the fifth fully connected layer transforms the previous 32 x 1 array into a 20736 x 1 array, which is then reshaped into a 9 x 9 x 236 array. CTr1 and CTr2 use a 2 x 2 upsampling, followed by a 2 x 1 upsampling for the remaining layers. In order to preserve the original image resolution, the first and last columns were removed after the CTr2 upsampling to form a 36 x 34 multichannel
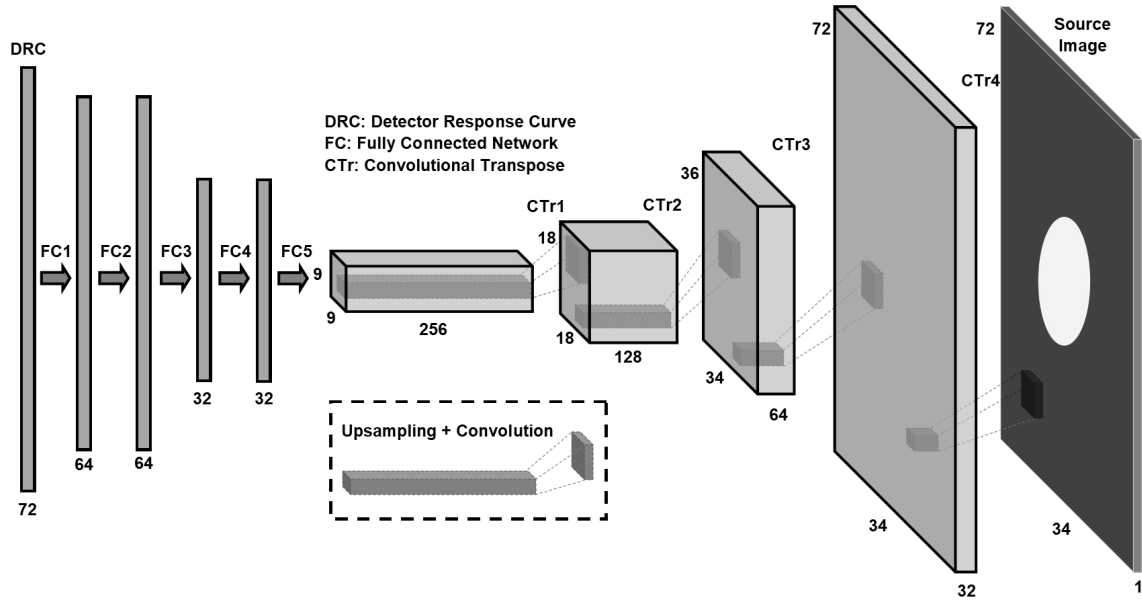
Figure 3: Architecture for the regenerative neural network (ReGeNN) used to convert the DRC back into the source image. ReGeNN utilizes fully connected layers as an encoder followed by "convolutional transpose" layers as a decoder that upsamples back into the original image.
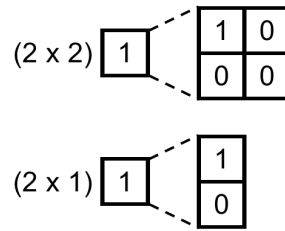

Figure 4: Upsampling method used for ReGeNN. A single pixel is converted into either a 2 x 2 or 2 x 1 array by keeping one pixel equal to the original value and setting the others to zero.

image. During upsampling, a single pixel is converted into a 2 x 2 or 2 x 1 array, with the top left pixel equal to the original pixel value and zero elsewhere (Figure 4). Each convolution uses a 3 x 3 filter, with the number of filters subsequently halved after each layer, until the final layer, which collapses all 32 layers into the final reconstructed image. A stride of one with zero padding on the edges was used to preserve the size after each convolution.

Each hidden layer used the ReLU activation function, defined as $f(z) = \max(0, z)$, while the final output layer used the sigmoid activation function, defined as $f(z) = 1/(1 + e^z)$. The decision to use the sigmoid activation function as the final layer was driven by defining each pixel to represent the relative source activity so that the range was constrained to [0,1]. Training was conducted in mini-batches of 128 samples each allowing batch normalization to be conducted after each activation function to improve convergence [26]. It was heuristically determined that setting the momentum for the batch normalization to 0.8 was ideal for this application (typical values are 0.9 - 0.99 for small batch sizes and 0.6 - 0.9 for large batches). Training was conducted using the Adam optimizer (an efficient

variant of stochastic gradient descent) with the learning rate set to 0.0001, $\beta_1 = 0.5$, and $\beta_2 = 0.999$ [27]. Readers knowledgeable on the Adam optimizer may note that $\beta_1 = 0.5$ is lower than what is typically recommended; the default value of 0.9 often resulted in training instability and was lowered based on another CNN architecture design to improve stability [28].

As the pixels in the original source image were either "on" or "off", the binary cross-entropy was chosen as the loss function to be optimized, defined as

$$\text{Loss} = -\sum_j \left(\hat{\lambda}_j \log(\lambda_j) + (1 - \hat{\lambda}_j) \log(1 - \lambda_j) \right), \tag{1}$$

where $\hat{\lambda}_j$ and λ_j are the true and reconstructed pixel values, respectively, with index j ranging over all pixels. The binary cross-entropy loss function proved more efficient over the standard mean-square error. When using the mean square error, the network would often converge to a monotonic image with each pixel set to 1/2448 (the total number of pixels), effectively averaging out the solution-space and converging to a local minimum.

3.2. Training Data

The specific source distributions are discussed in detail in the next section; in accordance with the previous ML-EM study, 5 unique shapes (4 distributed and 1 point source) were tested. The distributed sources spanned 5 discrete sizes ranging from $10° − 50°$ angular extent ($10°$ increments) as measured from the source's center. At a 72 x 34 image resolution, corresponding to $5°$-resolution in both the azimuthal and polar angle, a total of 2448 source directions were possible with 51,408 unique source variations in shape, size, and direction. Of these variations, 45,000 were included as part of the training data while the remaining 6408 were used as a validation set to ensure that the network was not over-fitting to the training data. The images and DRCs used to evaluate ReGeNN were not included in the training data to prevent biasing, providing a better representation for the generalizing capability of the network.

Training was conducted in mini-batches of 128 training images throughout each epoch (an epoch is defined as one complete run through all the training data). The training images used for each mini-batch were randomly sampled from the complete training set in each epoch to prevent biasing caused from any local clustering of similar source distributions in the mini-batch of a particular epoch. All training was conducted using the Keras platform, using Tensorflow as the backend [29]. It is recommended for networks of this size to use the GPU as the processing unit, with this study finding a 10-fold decrease in run time when using a 1280 CUDA core GPU over a quad core 4 GHz CPU. A repository with the code used to construct, train, and evaluate ReGeNN is available, as ReGeNN may readily be applied to similar time-encoded techniques with minor adjustments to the input/output size and may be used as a foundation for other imaging techniques [30].

3.3. Performance Criteria

An analysis of variance (ANOVA) was conducted to determine the most significant factors associated with Re-GeNN performance and to provide a quantitative comparison to the ML-EM study, which goes into further detail on ANOVA principles [18]. For the purpose of this work, it is important to note that ANOVA is a statistical test that compares two or more population means using the probability of the measured variances, denoted by the p-value. ANOVA can be used to generate a predictive model of the mean; for example, the quadratic model can be defined as

$$y = c_1 x_1 + c_2 x_2 + c_{12} x_1 x_2 + c_{11} x_1^2 + c_{22} x_2^2 + \text{BIAS}, \tag{2}$$

where x_1 and x_2 are chosen factors to predict the mean value, y. The constants of proportionality c_1 and c_2 represent the first-order effects, c_{12} represents the first-order interaction effect, and c_{11} and c_{22} represent the second-order effects. Under the null hypothesis, the mean is invariant to the factor effects, with the constants of proportionality equal to zero. For this study, any factor with a p-value less than 0.10 was deemed statistically significant.

Three factors were chosen to test under ANOVA: the source's 1) shape, 2) size, and 3) center polar angle. The four shapes tested, plotted in Figure 5, were chosen to mimic realistic source distributions:

1. Disc: Corresponding to a cross-section of a cylinder or sphere. This mimics nuclear waste containers used in storage as well as spherical forms of special nuclear material.

2. Ring: Corresponding to a hollow cylinder. This mimics contaminated storage drums as well as the annular shape commonly used to store special nuclear material.

3. Junctions ("X" shape): Used to simulate contaminated pipes or multiple fuel rods.

4. Square: Used to capture sharp corners that are not available in the other images. Extensions of this shape include rectangles that mimic the cross-section of cylinders including straight pipes, fuel rods, and waste storage drums.

The source size was defined as the maximum angular extent referenced from the source's center direction, with 2 discrete values of 30° and 50° chosen to be included in the ANOVA test. Finally, the source direction was defined as the source's center polar angle direction, with 3 discrete values of $\phi = 30°$, 90°, and 150° included in the ANOVA test. These factor levels correspond to the previous ML-EM study, allowing for a one-to-one comparison between the two algorithms. A full factorial model was conducted, corresponding to 24 unique source distributions. Three point sources were included at the designated polar angles, but were not included in the ANOVA to prevent biasing (point sources, by definition, do not have a size).
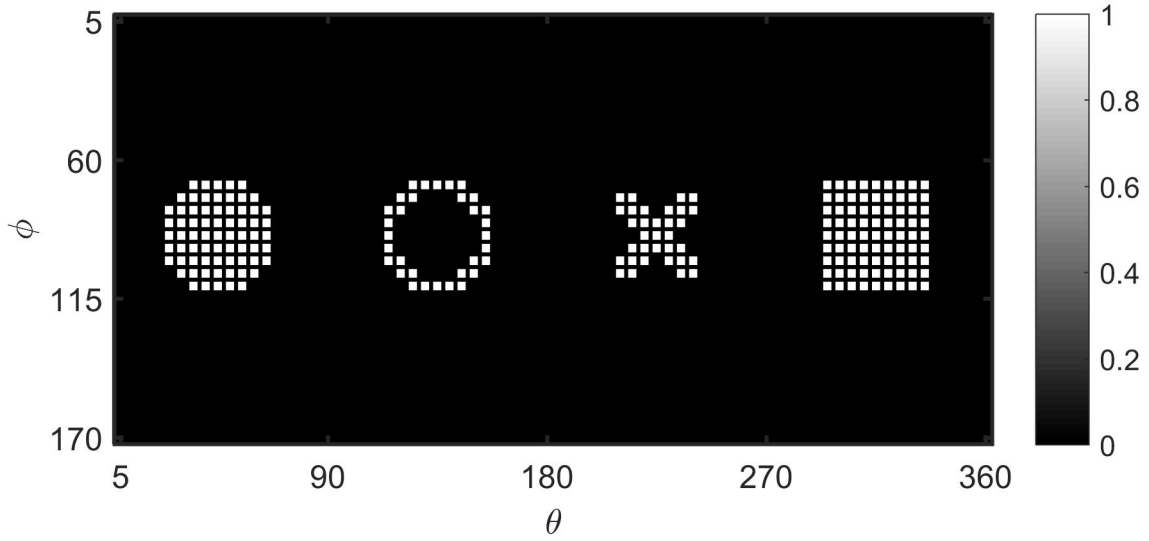
7

Figure 5: From left to right the four source shapes used: disc, ring, junction, and square (examples shown use a 40° angular extent, with the center polar angle at 90°). In this study, the mathematical convention for spherical coordinates was used where ϕ is the polar angle and θ is the azimuthal angle. The color scale indicates the pixel's relative activity.

Having defined the factors, the performance criteria were defined with the following figures of merit (FOM):

$$E = \frac{\sum_j |\hat{\lambda}_j - \lambda_j|}{\sum_j \hat{\lambda}_j}, \tag{3}$$

$$\text{Precision} = \frac{\sum_j \hat{\lambda}_j \lambda_j}{\sum_j \lambda_j}, \tag{4}$$

$$\sigma = \sqrt{\frac{1}{N} \sum_{j=1}^{N} \left(\hat{\lambda}_j \lambda_j - \mu\right)^2}, \tag{5}$$

where E is the relative error between the true and reconstructed images, precision is defined as the ratio of total activity contained within the region of interest compared to the background within the reconstructed image, and σ is defined as the standard deviation within the reconstructed image region of interest (ROI). For this study, the ROI was defined as the pixels corresponding to the original source distribution, and μ was defined as the average value of $\hat{\lambda}_j \lambda_j$ within the ROI. The equations assume that the images have been normalized to maximum activity, and the original source distribution is monotonic (uniform activity). An ideal image would have low relative error, high precision, and low standard deviation.

Astute observers may note that the convergence time has been excluded when comparing to the ML-EM analysis. However, unlike ML-EM, where the convergence time directly corresponds to the post-processing wait time for
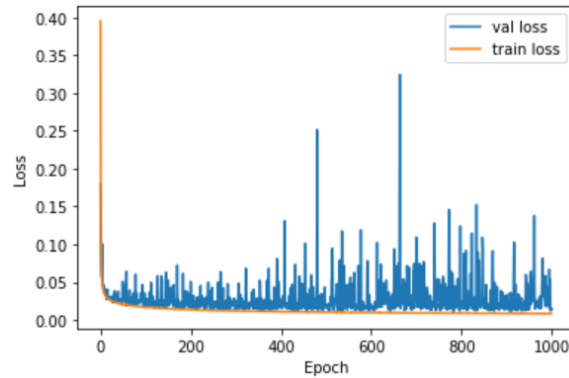
Figure 6: ReGeNN training history using the 45,000 ideal DRCs as the training set (values shown are the average loss value after each epoch). While both the training and validation curves both converge towards zero, the spikes in the validation set indicate some potential over-fitting or instabilities in the training process.

predicting an image after measurement, the training in ReGeNN is completely pre-processed. After the network has been trained, the image reconstruction is near-instantaneous, providing *real-time* analysis. This is an automatic benefit gained from using a neural network over other iterative techniques.

4. Results

4.1. Neural Network Training

ReGeNN was trained over 1,000 epochs, equating to 352,000 total updates to the network when using the mini-batch mode. The training history is plotted in Figure 6, along with the validation history after each epoch. These plots are used to verify that the network is training appropriately and converging to a solution (training loss trends towards zero) without over-fitting (validation loss trends towards zero equally with the training loss). The plot shows that both loss values are converging towards a solution, although there appears to be many instabilities within the validation set, as indicated by the sharp spikes present in the validation loss curve. These instabilities are likely caused by the stochastic method by which the network is being trained on, with each spike corresponding to a small perturbation from a local minima.

Visually comparing the original source distributions (Figure 7a) and the ReGeNN reconstructions after 1,000 epochs (Figure 7b) show remarkable agreements. Only two images deviate significantly (visually) from the original: the point source and large ring located at $\phi = 150°$, with the former identifying a completely different point source direction and the latter generating a secondary "phantom" ring source near the top of the image. However, the overall excellent agreement between the two figures shows that ReGeNN converged properly as none of these images were included in the training, demonstrating the network's generalizing capabilities. Considering these results, it is likely

9

Table 1: FOM ANOVA for ReGeNN Reconstructions

Factor	p-value		
	E	Precision	σ
Shape	**< 0.0001**	**< 0.0001**	**0.08**
Size	0.30	0.11	0.91
Direction	0.74	0.90	0.77
Shape*Size	0.93	0.87	0.78
Shape*Direction	0.92	0.59	0.69
Size*Direction	**0.02**	**0.02**	0.23
Direction^2	0.39	0.38	0.14

that that the large spikes in the validation history may be caused by only a few poor performing images, as the binary cross-entropy is logarithmic and can take on an extremely high value from just relatively few bad pixels.

4.2. Image Reconstruction ANOVA

The ANOVA results for the 24 distributed sources of Figure 7 are presented in Table 1. These results show that most factors had p-values significantly larger than the 0.10 threshold chosen, so that the null hypothesis that they have no effect on the mean could not be rejected. However, the shape had p-values less than 0.10 for all three FOM, while the shape/direction interaction term (denoted by *) also fell below the significance threshold for the relative error and precision. Thus, the null hypothesis may be rejected, and there is statistical support that these factors have an effect in their respective FOM. It should be noted that some p-values, such as the size term for precision and direction-squared term for σ, are close to the threshold and may warrant further investigation in future studies regarding RSM design. For this study, the ANOVA was deemed sufficient when considering the overall improvement in reconstructing the source distributions.

To understand how these factors affected the FOM, each model was fit using a least squares regression of just the significant factors. For example, the model for the relative error would be given by

$$E = c_{\text{Disc}} + c_{\text{Ring}} + c_{\text{Junction}} + c_{\text{Square}} + c_1 \left(\frac{\text{Size} - 40°}{10°} \right) \left(\frac{\text{Direction} - 90°}{60°} \right) + \text{BIAS}, \tag{6}$$

where the constant of proportionality for the shape has been broken into each categorical factor and c_1 is the size/direction interaction constant. Under this model, the bias roughly approximates the average expected FOM. When calculating the FOM with this model, only one categorical factor would be used, with the other constants of proportionality being set to zero. Finally, the terms in parentheses have been mapped to the range [-1,1] for the factor levels provided. In this way, all constants of proportionality are equally scaled and reflect the relative importance for each factor. These models are summarized in Table 2; for simplicity, only the significant factors are included with "–" indicating that the

(a) True Source Images

(b) ReGeNN

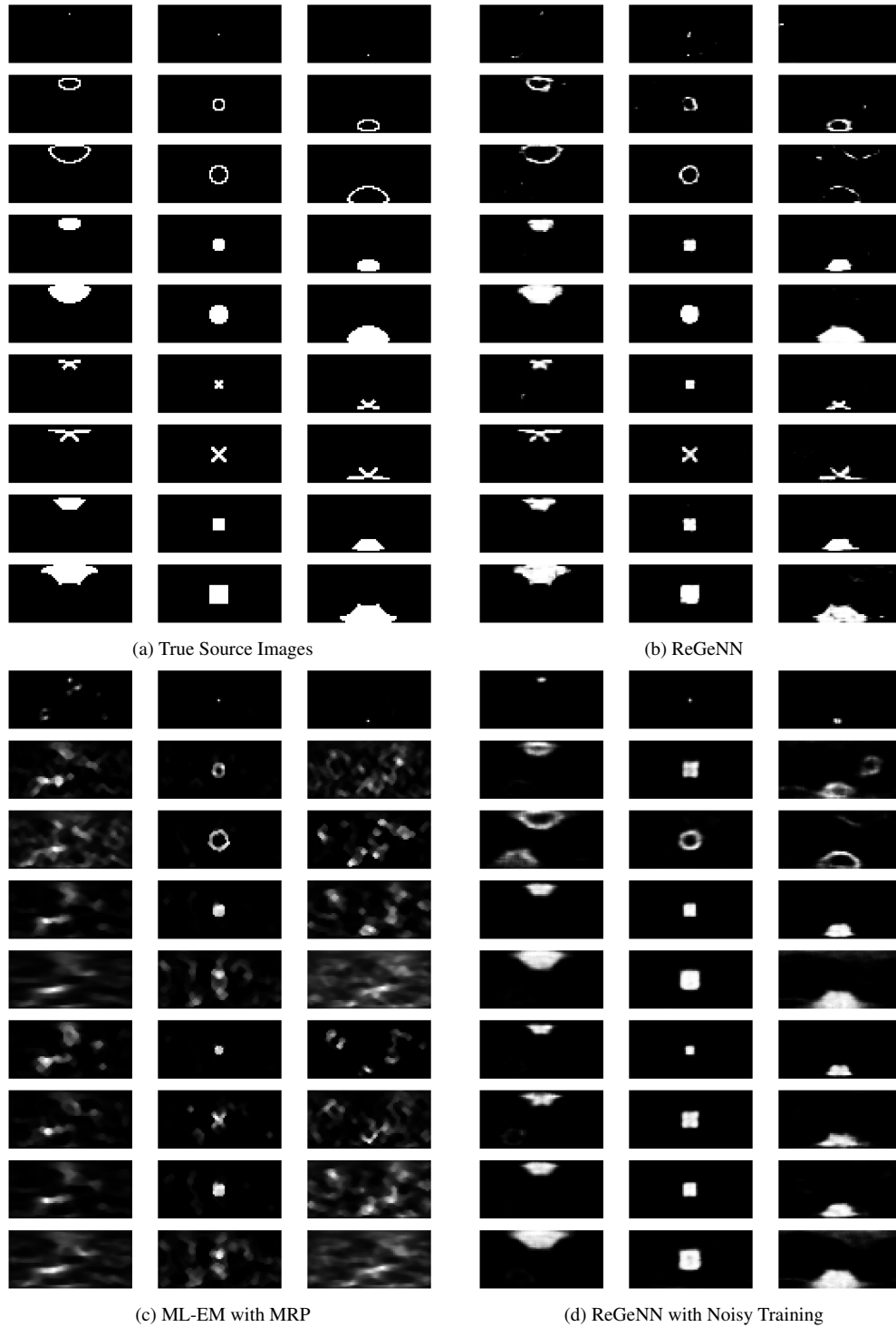(c) ML-EM with MRP

(d) ReGeNN with Noisy Training

Figure 7: Comparing the (a) true source distributions with (b) ReGeNN reconstructions shows significant improvement over (c) ML-EM with MRP, with ReGeNN recreating the source distribution at much higher detail over all source types. (d) Adding noise into the training data does not significantly impact the reconstructions, with the primary effect being blurring of sharp edges.

Table 2: Predictive Modeling using Significant Factors from ReGeNN ANOVA

Factor	Proportionality Constant		
	E	Precision	σ
Disc	-0.18	+0.09	–
Ring	+0.43	-0.23	+0.08
Junction	–	–	–
Square	-0.20	+0.12	–
Size	–	–	–
Direction	–	–	–
Shape*Size	–	–	–
Size*Direction	+0.10	-0.05	–
Direction^2	–	–	–
Bias	+0.29	+0.86	+0.20

factor does not impact the FOM.

When the categorical shapes were broken into their constitute components, the junction shape was determined to not significantly impact any FOM. The disc and square sources generally improved performance, lowering the relative error to as small as 9% and increasing the precision to as much as 98%. However, the ring sources were shown to have an inverse effect as reconstructions from those shapes had larger relative error, lower precision, and higher standard deviation (i.e. noise) within the ROI. It is also interesting to note that the ring reconstructions were the only ones that affected the standard deviation. Finally, the size/direction interaction term indicates ReGeNN under performed for sources with a larger size and near the southern pole of the RSM ($\phi = 150°$).

These results supports the visual comparisons between Figures 7a and 7b. The disc, junction, and square source distributions are generally reconstructed in high detail and accuracy regardless of their size or direction, while the disc reconstructions are not as uniform as the original source shape. The right column, corresponding to $\phi = 150°$, also contain more phantoms than the other two ϕ directions, particularly for the large disc and, to a lesser extent, the larger square source. This is quantified in Tables 1 and 2 through the size/direction interaction term. Through both quantitative and qualitative analysis, it is therefore possible to conclude that only the shape and combined size/direction of the source distribution significantly affects reconstruction quality for ReGeNN.

4.3. Training for Noise

Following the success training ReGeNN under ideal conditions, ReGeNN was retrained using noisy DRCs to test its capabilities for more realistic applications. With this test, 10 "noisy" DRCs were generated for every possible source distribution by sampling each point along the DRC with a Gaussian distribution (the Gaussian was determined to be sufficient to approximate Poisson counting statistics given the number of expected counts in realistic scenarios). Each Gaussian was generated with a 2% relative standard deviation, using the ideal DRC as the mean value; the
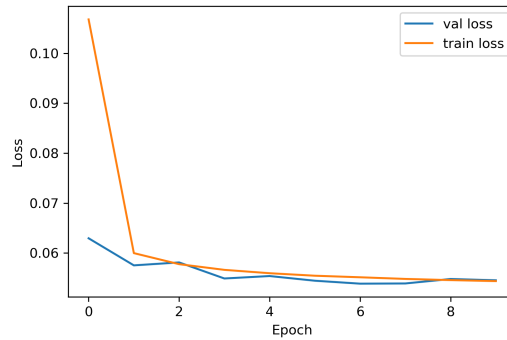
Figure 8: ReGeNN training history using 514,080 noisy DRCs as the training set. While fewer epochs and less updates to the network were conducted compared to the ideal training, the training and validation sets both converged towards zero.

corresponding source image was kept to be the same monotonic activity from before. This generated a total of

210 514,080 DRCs to retrain ReGeNN, and another full set of 51,408 noisy DRCs were used as a validation set. All hyper-parameters previously described were kept the same, except the number of epochs was lowered to 10 due to the larger training data set. While this corresponded to $\approx$ 10x less updates than before, the training history in Figure 6 shows that 1000 epochs was not necessary. The solution converged after about 100 epochs, thereby driving the decision to lower number of epochs for this training.

215 The training history using the noisy data set is plotted in Figure 8. As before, both the training and validation sets trended towards zero, indicating that the network was appropriately training towards a global solution. Although not as many epochs were conducted, the larger data sets smoothed the validation loss curve, removing the spikes from the validation set that were previously seen under the ideal DRC training. Reconstructions with this noisy training and using the ideal DRCs as the input are presented in Figure 7d.

220 The reconstructions again show excellent overall agreement, at a slight cost to blurring edges and loss of finer details. This loss is most notable for the junction sources, although some features remain to distinguish them from the disc and square source distributions, which are harder to discern. This is a relatively intuitive result as the difference between the square and disc distributions is only a few pixels and even a minor amount of noise is enough to complicate the reconstruction process. Phantoms are also present, but not noticeably more than before under the ideal training. It

225 is interesting to note that training ReGeNN with noisy data helped clean the reconstructions for point sources, even if the reconstructions are not perfect "points". In general, these results show that ReGeNN is capable of handling noisy inputs for practical applications without minimal loss of source information in the reconstruction.
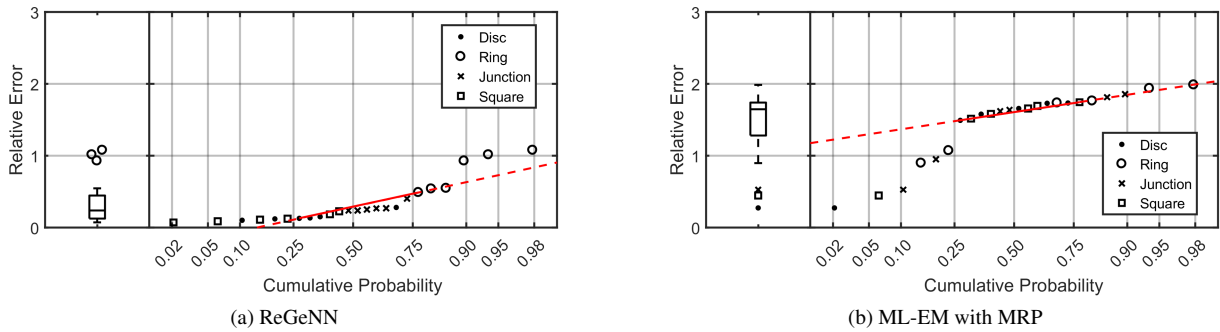
(a) ReGeNN

(b) ML-EM with MRP

Figure 9: Comparing the relative error for the distributed sources using ReGeNN and ML-EM with MRP. The plots show that ReGeNN has an overall higher accuracy and consistency than ML-EM, decreasing the average relative error from 145% ± 49% to only 33% ± 29% (reporting one standard deviation).

4.4. Comparison to ML-EM

The analysis will conclude with a brief comparison between ML-EM and ReGeNN. The performance is readily summarized in Figures 9 and 10, which plots the relative error for the 24 distributed sources as a box plot and a normal probability plot for the 3 reconstruction methods tested. The probability axis is scaled such that any normal distribution would appear linear; superimposed on the plots are solid lines connecting the first and third quartiles, with dashed lines extrapolating it to the extremes. Under the null hypothesis, the FOM would be equal with some normally-distributed noise accounting for any variance so that most of the data would fall along the superimposed line. Thus, these plots are used for quick factor-screening (and model-assurance) by looking at the shape of the data and if any fall outside of the normal distribution.

The ANOVA conducted already accounts for the outliers shown in the plots. What is most significant about these figures are the mean and spread of the data; ML-EM had an average relative error of 145% ± 49% , while ReGeNN under ideal training had only 33% ± 29% (reporting one standard deviation). Reconstruction using ReGeNN had an average value lower than even the best reconstructions from ML-EM. This is a significant improvement across the full phase space tested that was not fully anticipated. Previous measurements indicated performance near the poles may be degraded, resulting in a more limited FOV than desired. However, ReGeNN had only a minor dependence on the source direction (as a secondary interaction effect with source size). Unlike ML-EM, which depended heavily on the direction-squared term, the biggest factor in ReGeNN was the source shape.

Using noisy data did degrade performance, as shown in Figure 10, but primarily for the ring reconstructions; all other source distributions were reconstructed better than the majority of reconstructions from ML-EM. This did result in a larger mean relative error, at 83 ± 66%, although it maintained reasonable visual quality and accurate source location and spatial extent information.

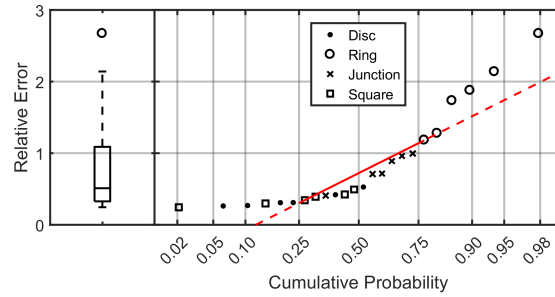Table 3 summarizes the various methods over the distributed sources, giving the average value for each FOM and

Figure 10: Normal probability plot for ReGeNN trained with noisy DRCs.

Table 3: Comparing Performance between Reconstruction Algorithms

Method	Average FOM		
	E	Precision	σ
ML-EM with MRP	$145 \pm 49\%$	$27 \pm 25\%$	$12 \pm 7\%$
ReGeNN with Ideal	$33 \pm 29\%$	$85 \pm 16\%$	$24 \pm 8\%$
ReGeNN with Noise	$83 \pm 66\%$	$64 \pm 22\%$	$14 \pm 6\%$

their standard deviation among the reconstructions. ReGeNN trained under ideal conditions performed the best in all categories except for σ, although the value for ML-EM is artificially low as most reconstructions failed in general and thus had low values for $\hat{\lambda}_j \lambda_j$. The standard deviation within the ROI did decrease when ReGeNN was trained using noisy data, a result of the network blurring the images and removing some finer details. Both ReGeNN models outperformed ML-EM significantly, with the ideal scenario having better FOM and more consistency between the various source distributions.

5. Conclusion

This study presented an alternative, CNN-based reconstruction algorithm, known as ReGeNN, for RSM gamma imaging and other similar time-encoded detection systems. An RSM system using a Mace mask design was simulated in MCNP v6.1.4 to form a basis set of radiation source distributions and corresponding DRCs. The simulated results show that the trained ReGeNN could be used for RSM imaging, reducing the average relative error of the reconstructions to 33% and increasing the average precision to 85% when trained under ideal scenarios. For more realistic applications, the network was also shown to successfully reconstruct source distributions when trained with noisy data, with some minor degradation in the images. Both models outperformed ML-EM and suggests, for the first time, that imaging with the RSM system is not only plausible, but practical for application.

An ANOVA study concluded that the shape and size/direction interaction terms were the biggest factors affecting the reconstruction relative error and precision. Ring sources generally had the worst (but still reasonable) FOM, while larger sources directed near the southern pole of the RSM also slightly degraded performance. This is in direct

contrast to the ML-EM ANOVA, which discovered a large dependence based on the source's direction and size, with the algorithm generally failing to reconstruct most source distributions. Another significant advantage was that the reconstruction was near instantaneous for ReGeNN, as nearly all the computation time was due to training the algorithm, a pre-processing step performed before taking data. This method could have great potential applications towards nuclear security and safety where responsive feedback is necessary.

Furthermore, ReGeNN is not limited to just the RSM system, as the network could readily be adjusted for similar time-encoded systems with minimal changes to the network architecture. The techniques and methods may also be applied to other imaging applications, although careful consideration must be given when formatting the inputs and changing the network layers.

The results presented are only simulations, and a more rigorous experimental study is required to fully vetting and demonstrate the RSM imaging capabilities. Future work can explore experiments validation and expand upon methods to improve the performance of ReGeNN in statistics-limited scenarios. Additionally, future work can also investigate a thorough mask design optimization for imaging applications, with ReGeNN integrated into the model as the reconstruction algorithm, to improve the overall coupled system performance.

Acknowledgments

References

[1] M. Laraia, Nuclear Decommissioning: Planning, Execution and Decommissioning, Woodhead Publishing, 2012.

[2] P. Martin, N. Tomkinson, T. Scott, The future of nuclear security: Commitments and actions–power generation and stewardship in the 21st century, Energy Policy 110 (2017) 325–330.

[3] K. Vetter, R. Barnowksi, A. Haefner, T. H. Joshi, R. Pavlovsky, B. J. Quiter, Gamma-ray imaging for nuclear security and safety: Towards 3-d gamma-ray vision, Nuclear Instruments and Methods in Physics Research Section A: Accelerators, Spectrometers, Detectors and Associated Equipment 878 (2018) 159–168.

[4] I. Jovanovic, A. S. Erickson, Active Interrogation in Nuclear Security: Science, Technology and Systems, Springer, 2018.

[5] M. J. Cieślak, K. A. Gamage, R. Glover, Coded-aperture imaging systems: Past, present and future development–a review, Radiation Measurements 92 (2016) 59–71.

[6] D. Hellfeld, P. Barton, D. Gunter, L. Mihailescu, K. Vetter, A spherical active coded aperture for 4π gamma-ray imaging, IEEE Transactions on Nuclear Science 64 (11) (2017) 2837–2842.

[7] R. Zhang, P. Gong, X. Tang, P. Wang, C. Zhou, X. Zhu, L. Gao, D. Liang, Z. Wang, Reconstruction method for gamma-ray coded-aperture imaging based on convolutional neural network, Nuclear Instruments and Methods in Physics Research Section A: Accelerators, Spectrometers, Detectors and Associated Equipment (2019).

[8] C. G. Wahl, W. R. Kaye, W. Wang, F. Zhang, J. M. Jaworski, A. King, Y. A. Boucher, Z. He, The polaris-h imaging spectrometer, Nuclear Instruments and Methods in Physics Research Section A: Accelerators, Spectrometers, Detectors and Associated Equipment 784 (2015) 377–381.

[9] Y.-s. Kim, J. H. Kim, H. S. Lee, H. R. Lee, J. H. Park, J. H. Park, H. Seo, C. Lee, S. H. Park, C. H. Kim, Development of compton imaging system for nuclear material monitoring at pyroprocessing test-bed facility, Journal of Nuclear Science and Technology 53 (12) (2016) 2040–2048.

[10] Y.-S. Kim, J. H. Kim, J. Lee, C. H. Kim, Large-area compton camera for high-speed and 3-d imaging, IEEE Transactions on Nuclear Science 65 (11) (2018) 2817–2822.

[11] J. E. Goldsmith, M. D. Gerling, J. S. Brennan, A compact neutron scatter camera for field deployment, Review of Scientific Instruments 87 (8) (2016) 083307.

[12] K. Weinfurther, J. Mattingly, E. Brubaker, J. Steele, Model-based design evaluation of a compact, high-efficiency neutron scatter camera, Nuclear Instruments and Methods in Physics Research Section A: Accelerators, Spectrometers, Detectors and Associated Equipment 883 (2018) 115–135.

[13] J. G. FitzGerald, A rotating scatter mask for inexpensive gamma-ray imaging in orphan source search: Simulation results, IEEE Transactions on Nuclear Science 62 (1) (2015) 340–348.

[14] D. E. Holland, J. E. Bevins, L. W. Burggraf, B. E. O'Day, Rotating scatter mask optimization for gamma source direction identification, Nuclear Instruments and Methods in Physics Research Section A: Accelerators, Spectrometers, Detectors and Associated Equipment 901 (2018) 104–111.

[15] R. J. Olesen, B. E. O'Day, D. E. Holland, L. W. Burggraf, J. E. Bevins, Characterization of novel rotating scatter mask designs for gamma direction identification, Nuclear Instruments and Methods in Physics Research Section A: Accelerators, Spectrometers, Detectors and Associated Equipment (2018).

[16] B. V. Egner, Development of a mixed-radiation directional rotating scatter mask detection system, Master's thesis, Air Force Institute of Technology, Wright-Patterson AFB, OH (2019).

[17] J. V. Logan, D. E. Holland, L. W. Burggraf, J. A. Clinton, B. E. O'Day III, Monte carlo and experimental analysis of a novel directional rotating scatter mask gamma detection system, Nuclear Instruments and Methods in Physics Research Section A: Accelerators, Spectrometers, Detectors and Associated Equipment 947 (2019) 162698.

[18] R. J. Olesen, D. E. Holland, E. M. Brubaker, J. E. Bevins, Maximum likelihood reconstructions for rotating scatter mask imaging, Radiation Measurements (2020 (under review)).

[19] K. H. Jin, M. T. McCann, E. Froustey, M. Unser, Deep convolutional neural network for inverse problems in imaging, IEEE Transactions on Image Processing 26 (9) (2017) 4509–4522.

[20] J. Brennan, E. Brubaker, M. Gerling, P. Marleau, M. Monterial, A. Nowack, P. Schuster, B. Sturm, M. Sweany, Source detection at 100 meter standoff with a time-encoded imaging system, Nuclear Instruments and Methods in Physics Research Section A: Accelerators, Spectrometers, Detectors and Associated Equipment 877 (2018) 375–383.

[21] N. P. Shah, J. VanderZanden, D. K. Wehe, Design and construction of a 1-d, cylindrical, dual-particle, time-encoded imaging system, Nuclear

Instruments and Methods in Physics Research Section A: Accelerators, Spectrometers, Detectors and Associated Equipment (2019) 161785.

[22] X. Liang, X. Pang, D. Cao, D. Li, Z. Zhang, S. Liu, T. Hu, Y. Zhang, X. Wang, F. Meng, et al., Self-supporting design of a time-encoded aperture, gamma-neutron imaging system, Nuclear Instruments and Methods in Physics Research Section A: Accelerators, Spectrometers, Detectors and Associated Equipment 951 (2020) 162964.

[23] T. Kin, Y. Sanzen, M. Kamida, K. Aoki, N. Araki, Y. Watanabe, Artificial neural network for unfolding accelerator-based neutron spectrum by means of multiple-foil activation method, in: 2017 IEEE Nuclear Science Symposium and Medical Imaging Conference (NSS/MIC), IEEE, 2017, pp. 1–2.

[24] E. K. Elmaghraby, M. Tohamy, M. Comsan, Determination of isotopes activity ratio using gamma ray spectroscopy based on neural network model, Applied Radiation and Isotopes 148 (2019) 19–26.

[25] A. Dosovitskiy, J. T. Springenberg, M. Tatarchenko, T. Brox, Learning to generate chairs, tables and cars with convolutional networks, IEEE transactions on pattern analysis and machine intelligence 39 (4) (2016) 692–705.

[26] S. Santurkar, D. Tsipras, A. Ilyas, A. Madry, How does batch normalization help optimization?, in: Advances in Neural Information Processing Systems, 2018, pp. 2483–2493.

[27] D. P. Kingma, J. Ba, Adam: A method for stochastic optimization, arXiv preprint arXiv:1412.6980 (2014).

[28] A. Radford, L. Metz, S. Chintala, Unsupervised representation learning with deep convolutional generative adversarial networks, arXiv preprint arXiv:1511.06434 (2015).

[29] F. Chollet, et al., Keras, `https://keras.io` (2015).

[30] R. J. Olesen, et al., Regenn (Mar 2020). doi:10.5281/zenodo.3725845.
    URL `https://doi.org/10.5281/zenodo.3725845`